# Robustness Study of Optimal Geometries for Cooperative Multi-Robot Localization

Mathilde Theunissen, Isabelle Fantoni, Ezio Malis, Philippe Martinet

# Robustness Study of Optimal Geometries for Cooperative Multi-Robot Localization

Mathilde Theunissen[1,2], Isabelle Fantoni[1], Ezio Malis[2] and Philippe Martinet[2]

***Abstract*— This work focuses on localizing a single target robot with multi-robot formations in 2D space. The cooperative robots employ inter-robot range measurements to assess the target position. In the presence of noisy measurements, the choice of formation geometries significantly impacts the accuracy of the target robot's pose estimation. While an infinite number of geometries exists to optimize localization accuracy, the current practice is to choose the final formation geometry based on convenience criteria such as simplicity or proximity to the initial position of the robots. The former leads to the selection of regular polygon-shaped formations, while the latter results in behaviour-based formations. Different from existing works, we conduct a complete robustness study of formation geometries in the presence of deviations from the desired formation and range measurement errors. In 2D scenarios, we establish necessary and sufficient conditions for formation geometries to be robust against robot positioning errors. This result substantiates the extensive use of regular polygon formations. However, our analysis reveals the lack of robustness of the commonly used square formation geometry, which stands as an exception. Simulation results illustrate the advantages of these robust geometries in enhancing target localization accuracy.**

## I. INTRODUCTION

Autonomous mobile robots crucially require reliable and accurate localization. In the absence of GNSS reception, such requirements can be achieved at a centimeter-precision level using range or bearing measurements provided by wireless positioning sensor networks. The deployment of range-only positioning systems is the subject of this work.

Infrastructure-based positioning solutions aim to fix sensors, called anchors, in the environment. When equipping the infrastructure, it is essential to choose proper anchor geometries due to their significant impact on the accuracy of the target robot's position estimation. This phenomenon, known as Dilution Of Precision (DOP), has been characterized in [1]. The widely-used metric for assessing DOP is the *Position Dilution Of Precision* (PDOP) index, which indicates how noisy range measurements affect the estimated state of the target robot. Optimal anchor geometries are obtained by minimizing the PDOP. This minimization is NP-hard to solve [7] as it should reduce localization errors over the robot's workspace while minimizing the number of anchors [4] and taking into consideration non-line-of-sight sensors. Bayesian [8] and genetic [4], [5] algorithms combined with discrete optimization variables [6] have mainly been used.

[1]Nantes Université, École Centrale Nantes, CNRS, LS2N, UMR 6004, F-44000 Nantes, France, {mathilde.theunissen, isabelle.fantoni}@ls2n.fr

[2]INRIA Centre at Université Côte d'Azur, Sophia Antipolis, France, {philippe.martinet, ezio.malis}@inria.fr

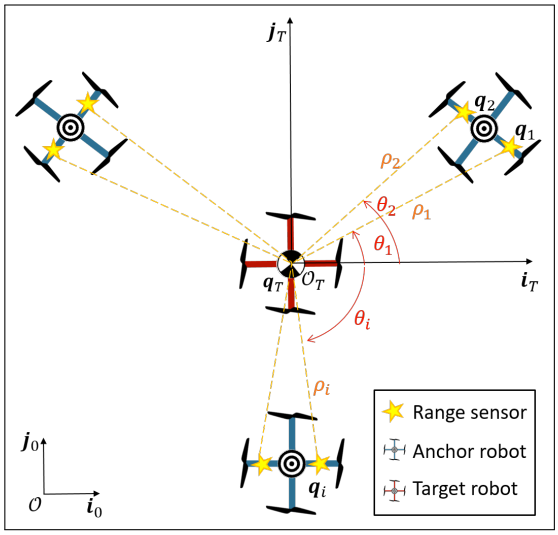


Fig. 1: A range-only positioning system comprises $N = 3$ robots with $M = 6$ sensors for localizing a target robot.

In large environments, fixed anchor networks suffer from several drawbacks. Firstly, the wider the workspace, the larger the search set and the more complex the optimization problem becomes. The optimality is traded for computation time to obtain a feasible solution [6]. Secondly, [5] shows that at least 3 line-of-sight anchors are necessary for estimating the target robot's position through trilateration. To avoid uncovered areas, a high density of anchors is inevitable. Finally, minimizing the number of anchors leads to large anchor-target distances. This reduces localization accuracy as it increases measurement noise [3] and multi-path effect [2].

In this work, we have chosen to embed anchors on mobile robots, as shown in Fig. 1, to avoid the previously mentioned drawbacks. A formation of anchor robots is deployed to track and localize a target robot. As anchor robots follow the target, the search for the optimal formation geometry is simpler than for fixed anchors because it eliminates the coverage problem. The formation geometry is then obtained by minimizing the PDOP at a single point – the position of the target. This minimization can be solved analytically. Its solutions have been fully characterized and classified in [9]. Furthermore, [9] highlights the existence of an infinity of optimal formation geometries.

Most of existing results have only been concerned with characterization of optimal sensor placements for localization tasks [9], [10], [17]. To the best of our knowledge, no study focuses on assessing the performance of optimal anchor placements. Consequently, the common practice considers

this infinity of optimal geometries to be equivalent. The formation used for localizing the target robot is then chosen based on subjective criteria such as simplicity or proximity to the robots' initial position. Indeed, N-regular polygons (2D) [10], N-regular polyhedrons (3D) [17], and cone configurations (3D) [12], [13] have been extensively studied due to their simplicity and symmetric properties. The proximity criterion gives rise to the behaviour-based formation control which uses artificial potentials to drive aerial formations to locally optimal formation geometries. In [18], such a field is constructed using the gradient of PDOP to drive flying anchor robots to the location that delivers optimal positioning service. Following the same idea, the artificial potentials of [19] attract the robotic system to a formation geometry that improves the localization accuracy of all robots. In both works, the gradient-descent approach makes the formation converge to the closest local minimum.

In this work, we question the common belief in the equivalence of the infinity of optimal geometries. We conduct our investigation through assessing the impact of mobile anchors' positioning errors on the target's state estimation. Indeed, for fixed anchor networks, these positioning errors are taken into account, and the resulting bias in the target localization is mitigated by calibration techniques, as in [11]. Our extensive robustness analysis shows that not all optimal geometries have the same robustness when experiencing a small deviation from their desired geometry. In the 2D setting, we characterize the necessary and sufficient conditions for PDOP-minimal formations to be robust against robot positioning errors. Our results show that regular polygon formations respect these conditions. Interestingly, we find a lack of robustness in the commonly used square formation. Simulation results illustrate our robustness study.

## II. PROBLEM STATEMENT AND THEORETICAL BACKGROUND

### A. Problem Statement

As presented in Fig. 1, we consider a collaborative localization mission in 2D space. $N$ anchor robots with $M$ range sensors distributed among them aim to localize a target robot in a global inertial frame $\mathcal{F}_0 = (\mathcal{O}, \mathbf{i}_0, \mathbf{j}_0)$.

Let ${}^0\mathbf{q}_i = [{}^0x_i, {}^0y_i]^\top, i \in \{1, ..., M\}$ denote the position of the anchor $i$ in the global frame $\mathcal{F}_0$. The unknown position of the target robot, ${}^0\mathbf{q} = [{}^0x, {}^0y]^\top$, is reconstructed from ranges $\rho_i, i \in \{1, ..., M\}$ between itself and the anchor $i$:

$$\rho_i = ||{}^0\mathbf{q}_i - {}^0\mathbf{q}|| = \sqrt{({}^0x_i - {}^0x)^2 + ({}^0y_i - {}^0y)^2} \quad (1)$$

We consider a coordinate change centered at ${}^0\mathbf{q}$. In this new frame $\mathcal{F}_T = (\mathcal{O}_T, \mathbf{i}_T, \mathbf{j}_T)$, the position of the anchor $i$ ${}^T\mathbf{q}_i = [{}^Tx_i, {}^Ty_i]^\top$ in $\mathcal{F}_T$ is expressed in polar coordinates:

$${}^T\mathbf{q}_i = [{}^0x_i - {}^0x, {}^0y_i - {}^0y]^\top = [\rho_i \cos\theta_i, \rho_i \sin\theta_i]^\top \quad (2)$$

where

$$\theta_i = \tan^{-1}\left(\frac{{}^0y_i - {}^0y}{{}^0x_i - {}^0x}\right) \quad (3)$$

denotes the polar angle of anchor $i$. In the remaining of this paper, all positions are expressed in $\mathcal{F}_T$. Therefore, the frame specification is omitted: ${}^T\mathbf{q}_i$ becomes $\mathbf{q}_i = [x_i, y_i]^T$.

### B. Assessing Localization Precision through the PDOP

In presence of noisy range measurements, the accuracy of the target robot's position estimation is evaluated by the PDOP [1]. This index is the ratio between the root mean square of the target robot's position estimation error and the range error variance. Under white noise measurements assumption, the PDOP is defined as:

$$PDOP := \sqrt{\mathrm{tr}((\mathbf{H}^\top\mathbf{H})^{-1})} = \sqrt{\frac{\mathrm{tr}(\mathbf{H}^\top\mathbf{H})}{\det(\mathbf{H}^\top\mathbf{H})}} \quad (4)$$

where $\mathbf{H}$ is the Jacobian matrix of (1):

$$\mathbf{H} = \begin{bmatrix} \frac{\partial\rho_1(x_1,y_1)}{\partial x_1} & \frac{\partial\rho_1(x_1,y_1)}{\partial y_1} \\ \vdots & \vdots \\ \frac{\partial\rho_M(x_M,y_M)}{\partial x_M} & \frac{\partial\rho_M(x_M,y_M)}{\partial y_M} \end{bmatrix} \quad (5)$$

Substituting (2) into (5) yields:

$$\mathbf{H} = \begin{bmatrix} \cos\theta_1 & \sin\theta_1 \\ \vdots & \vdots \\ \cos\theta_M & \sin\theta_M \end{bmatrix} \quad (6)$$

Consequently, $\mathbf{H}^\top\mathbf{H}$ is equal to:

$$\mathbf{H}^\top\mathbf{H} = \begin{bmatrix} \sum_{i=1}^{M}\cos^2\theta_i & \sum_{i=1}^{M}\cos\theta_i\sin\theta_i \\ \sum_{i=1}^{M}\cos\theta_i\sin\theta_i & \sum_{i=1}^{M}\sin^2\theta_i \end{bmatrix} \quad (7)$$

From (7), the trace of $\mathbf{H}^\top\mathbf{H}$ is a constant:

$$\mathrm{tr}(\mathbf{H}^\top\mathbf{H}) = \sum_{i=1}^{M}(\cos^2\theta_i + \sin^2\theta_i) = M \quad (8)$$

Furthermore, [14] shows that the determinant of $\mathbf{H}^\top\mathbf{H}$ can be written as:

$$\det(\mathbf{H}^\top\mathbf{H}) = \sum_{i,j>i}^{M}\sin^2(\theta_i - \theta_j) \quad (9)$$

By combining (8) and (9) with (4), we obtain the final expression of the PDOP:

$$PDOP = \sqrt{\frac{M}{\sum_{i,j>i}^{M}\sin^2(\theta_i - \theta_j)}} \quad (10)$$

From (10), we can see that the PDOP is a function of the **anchor geometry** parameterized by the polar angles $\boldsymbol{\theta} = [\theta_1, \ldots, \theta_M]^\top$. Note that the PDOP is independent of anchor-target distances $\rho_i$.

Therefore, the optimization problem, which aims to reduce the impact of noisy range measurements on the target robot's localization accuracy, is formulated as follows:

$$\boxed{\mathbb{O}_M := \arg\min_{\boldsymbol{\theta}} PDOP^2(\boldsymbol{\theta})} \quad (11)$$

We use the square of the PDOP to simplify further computations without loss of generality.

### C. An Infinity of Optimal Formation Geometries

By computing the critical points of (10), [15] and [16] demonstrate that formation geometries satisfy (11) if and only if:

$$\sum_{i=1}^{M} \sin(2\theta_i) = 0 \text{ and } \sum_{i=1}^{M} \cos(2\theta_i) = 0 \tag{12}$$

In the remaining of the paper, we refer to these optimal formation geometries as *PDOP minimizers*.

Under the conditions defined in (12), the computation of the determinant of $\mathbf{H}^\top\mathbf{H}$ shows that its upper bound is $\det(\mathbf{H}^\top\mathbf{H})^* = \frac{M^2}{4}$. Therefore, the minimal PDOP, denoted as $PDOP^*$, equals:

$$PDOP^* = \sqrt{\frac{M}{\frac{M^2}{4}}} = \frac{2}{\sqrt{M}} \tag{13}$$

The conditions of (12) result in an infinite number of PDOP minimizers for four reasons. Firstly, a new PDOP minimizer can be obtained by applying an identical rotation to all anchors of an optimal formation geometry. Secondly, distances between the target robot and the anchors have no effect on the optimality of the solution. Thirdly, central symmetries ($\theta_j = \theta_j + \pi$) with respect to the target robot position have no impact either. According to [17], these formation geometries are called *equivalent*. Finally, combinations of optimal geometries are also PDOP minimizers [9]. Indeed, given an arbitrary number of optimal geometries which satisfy (12), their combination verifies (12) too, regardless the combination choice. Interestingly, combinations and central symmetries lead to asymmetric optimal formation geometries.

## III. ROBUSTNESS ANALYSIS OF OPTIMAL FORMATION GEOMETRIES

### A. A Local Analysis of Robustness

In the case of mobile anchors, the target robot's localization accuracy depends on the deviation of the formation from its desired geometry. We conduct a complete robustness analysis of optimal geometries in presence of this deviation.

We work under the assumption of small perturbations, meaning that anchor deviations from their desired positions are small in comparison to their relative positions. Thus, we set the scope of this analysis to a local neighborhood of the optimal formation geometry.

### B. Robustness to Deviations from Optimal Geometry

A deviation of anchor $i$ from its desired position $\mathbf{q}_i^*$ can be divided into a polar angle error denoted by $\widetilde{\theta}_i$ and a distance error. As highlighted in section II-B, the PDOP function is completely independent of distances. Therefore, we analyse the impact of polar angles deviations only.

We consider that anchors' polar angles relative to the target $\boldsymbol{\theta} = [\theta_1, \ldots, \theta_M]^T$, are the summation of the desired polar angles $\boldsymbol{\theta}^* = [{\theta_1}^*, \ldots, {\theta_M}^*]^\top \in \mathbb{O}_M$, and the angular errors $\widetilde{\boldsymbol{\theta}} = [\widetilde{\theta_1}, \ldots, \widetilde{\theta_M}]^\top$:

$$\boldsymbol{\theta} = \boldsymbol{\theta}^* + \widetilde{\boldsymbol{\theta}} \tag{14}$$

We introduce the bias $\Delta PDOP^2$ which corresponds to the difference between the actual and the desired $PDOP^2$:

$$\Delta PDOP^2 = PDOP^2(\boldsymbol{\theta}) - PDOP^2(\boldsymbol{\theta}^*) \tag{15}$$

Under the small perturbations assumption, we approximate $\Delta PDOP^2$ using the second order Taylor expansion:

$$\Delta PDOP^2 \approx \frac{\partial PDOP^2}{\partial \boldsymbol{\theta}}(\boldsymbol{\theta}^*)\,\widetilde{\boldsymbol{\theta}} + \frac{1}{2}\widetilde{\boldsymbol{\theta}}^\top \frac{\partial^2 PDOP^2}{\partial \boldsymbol{\theta}^2}(\boldsymbol{\theta}^*)\,\widetilde{\boldsymbol{\theta}} \tag{16}$$

Since $\boldsymbol{\theta}^* \in \mathbb{O}_M$, then $\boldsymbol{\theta}^*$ is a minimum. Therefore, the gradient of the PDOP at $\boldsymbol{\theta}^*$, $\frac{\partial PDOP^2}{\partial \boldsymbol{\theta}}(\boldsymbol{\theta}^*)$, is null. We get:

$$\Delta PDOP^2 \approx \frac{1}{2}\widetilde{\boldsymbol{\theta}}^\top \mathbf{G}(\boldsymbol{\theta}^*)\,\widetilde{\boldsymbol{\theta}} \tag{17}$$

where $\mathbf{G} = \frac{\partial^2 PDOP^2}{\partial \boldsymbol{\theta}^2}$ is the Hessian matrix of size $(M \times M)$.

**Remark 1.** *Given a value of $\|\widetilde{\boldsymbol{\theta}}\|$, the bias $\Delta PDOP^2$ reaches its maximum value, $\frac{1}{2}\|\widetilde{\boldsymbol{\theta}}\|^2\lambda_{max}$, when the direction of $\widetilde{\boldsymbol{\theta}}$ is collinear to the eigenvector of $\mathbf{G}$ associated with its maximal eigenvalue $\lambda_{max}$.*

Consequently, the objective is to reduce the maximal eigenvalue of $\mathbf{G}$ to the smallest possible value while keeping the PDOP to its lower bound. In summary, we aim to solve:

$$\boxed{\begin{array}{c}\mathbb{O}'_M := \arg\min_{\boldsymbol{\theta}^*} \lambda_{max} \\ \text{subject to } \boldsymbol{\theta}^* \in \mathbb{O}_M\end{array}} \tag{18}$$

We characterize the eigenvalues of $\mathbf{G}$, in order to find the minimal value of $\lambda_{max}$. As shown in Appendix A, the matrix $\mathbf{G}$ at $\boldsymbol{\theta}^*$ is:

$$\mathbf{G}(\boldsymbol{\theta}^*) = \frac{32}{M^3} \cdot \begin{pmatrix} 1 & c_{12} & \ldots & c_{1M} \\ c_{21} & 1 & \ldots & c_{2M} \\ \vdots & \vdots & \ddots & \vdots \\ c_{M1} & c_{M2} & \ldots & 1 \end{pmatrix} \tag{19}$$

where $c_{ij} = \cos(2\theta_i^* - 2\theta_j^*) = c_{ji}$.

The symmetric matrix $\mathbf{G}$ has the following properties :

1) **Constant trace:** $\mathrm{tr}(\mathbf{G}) = \frac{32}{M^2}$. Thus, the sum of the eigenvalues of $\mathbf{G}$ is constant for all $\boldsymbol{\theta}^* \in \mathcal{O}_M$.
2) **Rank-deficiency:** $\mathrm{rank}(\mathbf{G}) \leq 2$. The complete demonstration is provided in Appendix B.

As a result, $\mathbf{G}$ has at most 2 non-zero eigenvalues $\lambda_{min}$ and $\lambda_{max}$ linked by the trace of $\mathbf{G}$.

$$\lambda_{max} = \frac{32}{M^2} - \lambda_{min} \tag{20}$$

According to (20), the minimal value of $\lambda_{max}$ is equal to $\frac{16}{M^2}$ when $\lambda_{max} = \lambda_{min}$.

**Theorem 1.** *A PDOP minimizer $\boldsymbol{\theta}^* \in \mathbb{O}_M$ belongs to the set $\mathbb{O}'_M$, if and only if :*

$$\begin{cases} \sum_{i=1}^{M} \cos^2(2\theta_i^*) = \frac{M}{2} \\ \sum_{i=1}^{M} \cos(2\theta_i^*)\sin(2\theta_i^*) = 0 \end{cases} \Leftrightarrow \begin{cases} \sum_{i=1}^{M} \cos(4\theta_i^*) = 0 \\ \sum_{i=1}^{M} \sin(4\theta_i^*) = 0 \end{cases}$$

The purpose of Theorem 1 is to guarantee that any formation geometry $\boldsymbol{\theta}^* \in \mathbb{O}'_M$ is robust to anchors positioning errors through the minimization of $\Delta PDOP^2$. Only a subset of $\mathbb{O}_M$ has this property. Consequently, not all PDOP minimizers have the same performance in terms of robustness against positioning errors. We provide the demonstration of Theorem 1 in Appendix C.

### C. The Particular Case of Regular Polygons

Here, we show that almost all *M-sided regular polygons* belong to the set of robust optimal formation geometries $\mathbb{O}'_M$. A property of M-sided regular polygons is that $\theta_k = \frac{2\pi}{M}k$. Therefore, the necessary conditions of Theorem 1 become:

$$\begin{cases} \sum_{k=1}^{M} \cos(4\theta_k) = \mathcal{R}e\left(\sum_{k=1}^{M}\left(\exp^{\frac{8\pi}{M}j}\right)^k\right) \\ \sum_{k=1}^{M} \sin(4\theta_k) = \mathcal{I}m\left(\sum_{k=1}^{M}\left(\exp^{\frac{8\pi}{M}j}\right)^k\right) \end{cases} \tag{21}$$

The geometric series in (21) can be simplify if $M \neq 4$ (for which the denominator of (22) cancels):

$$\begin{cases} \sum_{k=1}^{M} \cos(4\theta_k) = \mathcal{R}e\left(\frac{1-\exp 8\pi j}{1-\exp\frac{8\pi j}{M}}\right) = 0 \\ \sum_{k=1}^{M} \sin(4\theta_k) = \mathcal{I}m\left(\frac{1-\exp 8\pi j}{1-\exp\frac{8\pi j}{M}}\right) = 0 \end{cases}, \forall M \neq 4 \tag{22}$$

**Property 1.** *When $M \neq 4$, M-sided regular polygons, are solutions of $\mathbb{O}'_M$.*

The particular case of $M = 4$ gives:

$$\sum_{k=1}^{4} \cos(4\theta_k) = \sum_{k=1}^{4} \cos(2\pi k) = M \neq 0 \tag{23}$$

Therefore, the square formation $\notin \mathbb{O}'_4$. We can further show that in this case, the rank of $\mathbf{G}$ is equal to 1 (see Appendix B). Thus, $\mathbf{G}$ has a unique non-zero eigenvalue which is equal to $\frac{32}{M^2}$. The square formation corresponds to the worst geometry of $\mathbb{O}_4$ as $\lambda_{max}$ is maximal.

## IV. ANALYSIS OF PDOP CURVATURE

Section III presents the necessary and sufficient conditions on $\boldsymbol{\theta}^*$ for formations to be robust against anchors' deviation from their desired geometry. To completely define the formation, we seek the values of anchor-target distances. As the PDOP is distance independent, the common practice in wireless positioning networks is to choose homogeneous [10] and large anchor-target distances [22] to achieve better localization performance in presence of target localization uncertainty.

As seen in Sections II and III, measurement errors and formation deviation create a bias on the PDOP. A higher PDOP leads to an increase in the area $\mathcal{A}_T$ of the target's uncertainty ellipse. The semi-minor and semi-major axis of this ellipse correspond to the square roots of the eigenvalues of the target position covariance matrix $\mathbf{cov}(\widetilde{\mathbf{q}})$. Hence:

$$\mathcal{A}_T := \pi\sqrt{\det(\mathbf{cov}(\widetilde{\mathbf{q}}))} = \pi\sigma\sqrt{\det\left((\mathbf{H}^\top\mathbf{H})^{-1}\right)} \tag{24}$$

where $\sigma$ is the standard deviation of range measurement errors. By definition, $\mathbf{cov}(\widetilde{\mathbf{q}})$ is equal to $\sigma^2(\mathbf{H}^\top\mathbf{H})^{-1}$ [1]. Therefore, using (4), we obtain a proportional relation between the PDOP and the area $\mathcal{A}_T$:

$$\mathcal{A}_T = \frac{\pi\sigma}{\sqrt{\det(\mathbf{H}^\top\mathbf{H})}} \propto PDOP \tag{25}$$

An increase in the PDOP leads directly to an enlargement of $\mathcal{A}_T$. As the target robot is located within the uncertainty ellipse, the smaller the PDOP value in this ellipse, the more accurate the target position estimation. A smaller PDOP in the uncertainty ellipse is achieved by a smaller curvature of this function at $\mathbf{q}$, which is the center of the target uncertainty ellipse. The local PDOP curvature with respect to $\mathbf{q}$ is characterized by the Hessian matrix of the PDOP:

$$\frac{\partial^2 PDOP^2}{\partial \mathbf{q}^2} = \frac{32}{M^3}\begin{bmatrix} \sum_{i=1}^{M}\frac{\sin^2\theta_i}{\rho_i^2} & \sum_{i=1}^{M}\frac{\cos\theta_i\sin\theta_i}{\rho_i^2} \\ \sum_{i=1}^{M}\frac{\cos\theta_i\sin\theta_i}{\rho_i^2} & \sum_{i=1}^{M}\frac{\cos^2\theta_i}{\rho_i^2} \end{bmatrix} \tag{26}$$

Equation (26) is demonstrated in Appendix D. The two eigenvalues $\lambda_1$ and $\lambda_2$ of $\frac{\partial^2 PDOP^2}{\partial \mathbf{q}^2}$ are given by:

$$\lambda_{1,2} = \frac{16}{M^3}\left[\sum_{j=1}^{M}\frac{1}{\rho_j^2} \pm \sqrt{\left(\sum_{j=1}^{M}\frac{1}{\rho_j^2}\right)^2 - 4\sum_{j=1,k>j}^{M}\frac{\sin^2(\theta_j-\theta_k)}{\rho_j^2\rho_k^2}}\right] \tag{27}$$

By definition, the two eigenvalues $\lambda_1$ and $\lambda_2$ are the principal curvatures of the PDOP in the direction of their associated eigenvectors. In the special case where $\rho_1 = ... = \rho_M = \rho$, (27) becomes:

$$\lambda_1 = \lambda_2 = \frac{16}{\rho^2 M^2} \tag{28}$$

From (27) and (28), we can notice that the higher the distances $\rho_j$, the smaller the eigenvalues. Moreover, with homogeneous distances, both eigenvalues are equal.

**Property 2.** *Arc-shaped geometries, defined by $\rho_i = \rho_j \ \forall i,j \in \{1,\ldots,M\}$, with a high anchor-target distance and centered at the position of the target robot, improve the target localization accuracy.*

For arc-shaped formations, target position accuracy is barely affected by a biased PDOP. Property 2 demonstrates and justifies the observation of [22], who remarks that lengthening a wireless positioning network improves the overall localization precision. Note what, with most range sensors (e.g. UWB nodes), an increase in anchor-target distance induces noisier range measurements. A trade-off between noise and localization accuracy should be found.

## V. SIMULATION RESULT

In this section, we quantify the localization accuracy of the target using the PDOP due to its proportional relation with the target robot's uncertainty area, as shown in (25). Optimal formation geometries of $\mathcal{O}_M$ (resp. $\mathcal{O}'_M$) are obtained by solving (12) (resp. Theorem 1 with (12)) using the Newton-Raphson method or a gradient-descent optimization.

### A. Comparison between the Square and a $\mathbb{O}'_4$ Formation

We assess the performance of the square formation discussed in III-C in comparison with an optimal formation geometry $\mathcal{C}_4 \in \mathbb{O}'_4$. Both formations with their PDOP are shown in Fig. 2.

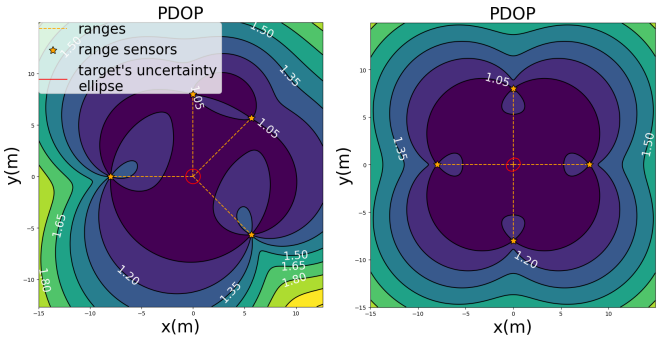


(a) $\mathcal{C}_4 \in \mathbb{O}'_4$ (b) Square configuration $\notin \mathbb{O}'_4$

Fig. 2: Contour maps for optimal $\mathcal{C}_4$ and square formations.

We introduce to the formation $\boldsymbol{\theta}$ a perturbation $\widetilde{\boldsymbol{\theta}}$ in the direction the eigenvector of $\mathbf{G}$ associated with $\lambda_{max}$. Fig. 3 shows the evolution of $\Delta PDOP$ with respect to the magnitude of $\widetilde{\boldsymbol{\theta}}$. For both formations, a larger $||\widetilde{\boldsymbol{\theta}}||$ results in a larger bias $\Delta PDOP$, evidenced by the upward trend in Fig. 3. As $\lambda_{max}$ is smaller for $\mathcal{C}_4$, the PDOP bias induced by $\widetilde{\boldsymbol{\theta}}$ is smaller for $\mathcal{C}_4$ than for the square formation. Thus, for the square formation, the target position is estimated with less precision as the target uncertainty ellipse increases.

The second experiment corresponds to a more realistic formation control scenario. We assume that the positioning error of each anchor robot $\widetilde{\boldsymbol{q}}_i$ follows a normal distribution $\widetilde{\boldsymbol{q}}_i \sim \mathcal{N}(0, \sigma_q^2)$. $\sigma_q$ has been chosen in order to have an error at $3\sigma_q$ equal to $1\text{m}$, which is a realistic error in formation control experiments. We inject this random noise to the position of the anchor robots for both formations and we measure the PDOP of the target. The result of 500 simulations is presented in Fig. 4.

Subject to this random noise, on average, both formations achieve similar performance in terms of accuracy, measured by the PDOP. This is explained by the fact that the two formations belong to the same super set $\mathbb{O}_4$.

On one hand, the square, with its single non-zero eigenvalue, performs better in the best case, where $\widetilde{\boldsymbol{\theta}}$ is far from the eigenvector associated with this non-zero eigenvalue. It leads to a slightly smaller median PDOP. On the other hand, the interquartile range is smaller for the $\mathcal{C}_4$ formation, leading to better performance in terms of repeatability and robustness. This smaller variance is explained by the fact that, $\mathcal{C}_4$ has two equal eigenvalues. Furthermore, with a smaller $\lambda_{max}$, $\mathcal{C}_4$ performs better in the worst case, where $\widetilde{\boldsymbol{\theta}}$ is collinear to the eigenvector associated with $\lambda_{max}$.

### B. Impact of Anchors Positioning Errors on Formations in $\mathbb{O}_M$ and $\mathbb{O}'_M$

In this section, we generalize the observations made in V-A for any $M$-anchor formations. We define $\mathcal{C}_M$, an optimal formation from $\mathbb{O}_M$ and $\mathcal{C}'_M$, an optimal formation from $\mathbb{O}'_M$. To have a fair comparison, we choose $\mathcal{C}_M$ and $\mathcal{C}'_M$ to be both arc-shaped geometries with the same anchor-target distance ($\rho = 7$).

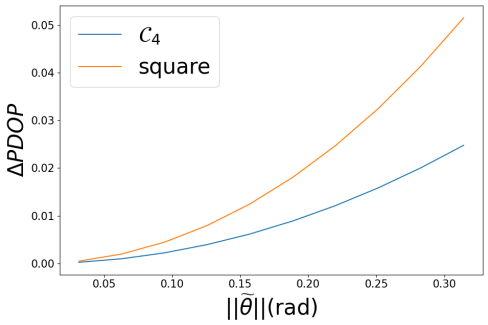


Fig. 3: Impact of a perturbation $\widetilde{\boldsymbol{\theta}}$ on the PDOP bias of the target robot localized by the $\mathcal{C}_4$ and the square formations.

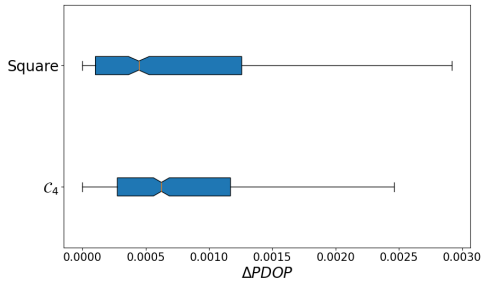


Fig. 4: Box plot representing the PDOP bias distribution in presence of a random noise on the positioning error of the anchor robots for the square and the $\mathcal{C}_4$ formations.

We choose to simulate the worst-case scenario where anchors positioning errors are collinear to the eigenvector of $\mathbf{G}$ associated with the $\lambda_{max}$ of each formation. The PDOP bias is then maximal. Our robust formation $\mathcal{C}'_M$ should outperform $\mathcal{C}_M$ in this scenario as the design of $\mathbb{O}'_M$ focuses on reducing the maximal PDOP bias. Simulation results are shown in Fig. 5 for different values of $M$, where the vertical axis denotes the difference between the PDOP of $\mathcal{C}_M$ and $\mathcal{C}'_M$.

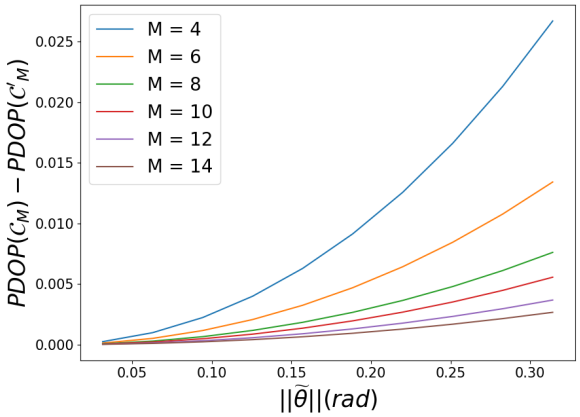


Fig. 5: PDOP difference between $\mathcal{C}_M$ and $\mathcal{C}'_M$ as function of $||\widetilde{\boldsymbol{\theta}}||$ for different values of $M$.

In Fig. 5, as $PDOP(\mathcal{C}_M) - PDOP(\mathcal{C}'_M) \geq 0$, formations $\mathcal{C}'_M$ are more robust to anchors positioning errors than $\mathcal{C}_M$ formations. We can also notice that the higher the number of anchors, the lower the difference between $PDOP(\mathcal{C}_M)$ and $PDOP(\mathcal{C}'_M)$. In other words, the smaller the number of anchors, the more beneficial are $\mathcal{C}'_M$ formations. The $\mathbb{O}'_M$ set is particularly useful in practical applications, where the number of anchors is usually smaller than $M = 10$.

### C. Impact of Anchor-Target Distance on Localization Uncertainty for $\mathbb{O}'_M$ Formation Geometries

In this section, we illustrate Property 2 stating that the higher the anchor-target distance, the flatter the curvature of the PDOP. Fig. 6 depicts PDOP contour lines in 2D space for two formations $\in \mathbb{O}'_6$ sharing the same geometry. In Fig. 6a, the formation $\mathcal{C}_{6,1}$ has a anchor-target distance of 6m, which is half the anchor-target distance of $\mathcal{C}_{6,2}$ in Fig. 6b.

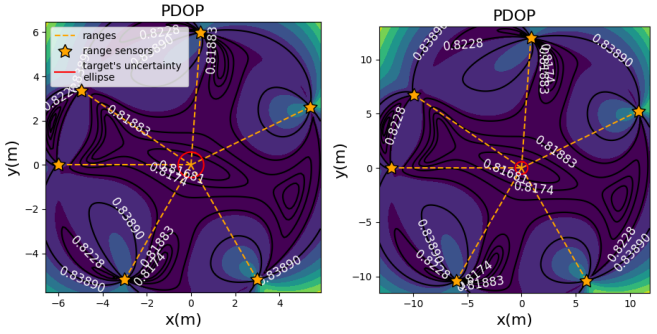


(a) $\mathcal{C}_{6,1} : \rho = 6$m (b) $\mathcal{C}_{6,2} : \rho = 12$m

Fig. 6: Two configurations of $\mathbb{O}'_6$ with different anchor-tag distances.

From Fig. 6, we observe that the PDOP curve is the same up to a scaling factor between $\mathcal{C}_{6,1}$ and $\mathcal{C}_{6,2}$. It might give the impression that the target uncertainty ellipse is larger for $\mathcal{C}_{6,1}$, which is a false impression as the x and y scale are different between the two subfigures. From the contour lines of Fig. 6, we notice that increasing anchor-target distance results in a flatter curvature of the PDOP. Therefore, at any point inside the red uncertainty ellipse, the value of the PDOP for $\mathcal{C}_{6,2}$ is smaller than for $\mathcal{C}_{6,1}$, except at the center where both PDOP values are identical. The target position estimation is more accurate for $\mathcal{C}_{6,2}$ compare to $\mathcal{C}_{6,1}$, thus attesting Property 2.

## VI. CONCLUSIONS

This paper explores the robustness of range-only positioning formations in the presence of anchors positioning errors. We provide the necessary and sufficient conditions for anchor robots' formations to be robust against formation deviations while minimizing the effects of range measurement noise. Even though the PDOP is independent of the anchor-target distances, we demonstrate the benefit of arc-shaped formation geometries with high anchor-target distances on the target robot positioning accuracy. Simulation results highlight the benefits of our approach particularly when dealing with a small number of anchors.

So far, we have underestimated the target localization uncertainty due to its approximation by the PDOP. Experimental validation is our next step to confirm the benefits of our robust formation geometries. We will equip robots in $\mathbb{O}_M$ and $\mathbb{O}'_M$ formations with ultra-wideband range sensors. In presence of positioning errors, the experimental accuracy and robustness of the target pose reconstruction using trilateration will be compared with theoretical predictions for both formations. Finally, we consider extending our work for 3D target tracking to develop heterogeneous cooperation between aerial and ground autonomous robots.

## APPENDIX

### A. Computation of the Hessian Matrix $\mathbf{G}$ at $\boldsymbol{\theta}^*$

To find the matrix $\mathbf{G}$, the first and second order derivatives of $\det(\mathbf{H}^\top\mathbf{H})$ are computed from (9) at point $\boldsymbol{\theta}^*$. At critical point $\boldsymbol{\theta}^*$, for which (12) holds, we obtain:

$$\begin{cases} \det(\mathbf{H}^\top\mathbf{H})(\boldsymbol{\theta}^*) = \frac{M^2}{4} \\ \frac{\partial \det(\mathbf{H}^\top\mathbf{H})}{\partial\theta_i}(\boldsymbol{\theta}^*) = 0 \\ \frac{\partial^2 \det(\mathbf{H}^\top\mathbf{H})}{\partial\theta_i^2}(\boldsymbol{\theta}^*) = 2\sum_{k=1}^{M}\cos(2\theta_i^* - 2\theta_k^*) - 2 = -2 \\ \frac{\partial^2 \det(\mathbf{H}^\top\mathbf{H})}{\partial\theta_i\theta_j}(\boldsymbol{\theta}^*) = 2\cos(2\theta_i^* - 2\theta_j^*) \end{cases} \tag{29}$$

Then, the coefficients of $\mathbf{G} = (\frac{\partial^2 PDOP^2}{\partial\theta_i\theta_j})_{1\leq i,j\leq M}$ are computed by applying the quotient rule to (10). We get:

$$\begin{cases} \frac{\partial^2 PDOP^2}{\partial\theta_i^2}(\boldsymbol{\theta}^*) = \frac{32}{M^3} \\ \frac{\partial^2 PDOP^2}{\partial\theta_i\theta_j}(\boldsymbol{\theta}^*) = \frac{32}{M^3}\cos(2\theta_i^* - 2\theta_j^*) \end{cases} \tag{30}$$

which leads us, in a matrix form, to (19).

### B. Rank of the Hessian Matrix $\mathbf{G}$ at $\boldsymbol{\theta}^*$

To determine the rank of $\mathbf{G}$ at point $\boldsymbol{\theta}^*$, we look for the number of independent equations of:

$$\mathbf{G}\left(\boldsymbol{\theta}^*\right).\mathbf{v} = \mathbf{0} \tag{31}$$

where $\mathbf{v} = [v_1, \ldots, v_M]^\top$ is the eigenvector of $\mathbf{G}$ associated with the null eigenvalue. This equation is equivalent to:

$$\sum_{i=1}^{M} c_{ji}v_i = 0, \forall j \in 1, \ldots, M \tag{32}$$

where $c_{ij} = \cos(2\theta_i^* - 2\theta_j^*)$. By applying to the $(M-1)$ last equations of (32) the trigonometric relation:

$$c_{ji} = c_{j1}c_{1i} - s_{j1}s_{1i} \tag{33}$$

where $s_{ij} = \sin(2\theta_i^* - 2\theta_j^*)$, we obtain:

$$\begin{cases} \sum_{i=1}^{M} c_{1i}v_i = 0 \\ s_{j1}\sum_{i=1}^{M} s_{1i}v_i = 0, j \in \{2, \ldots, M\} \end{cases} \tag{34}$$

On one hand, if $\forall j \in \{2, \ldots, M\}, \sin(2\theta_j^* - 2\theta_1^*) = 0$, then $\cos(2\theta_1^* - 2\theta_j^*) = 1$. The system (34) simplifies to:

$$\sum_{i=1}^{M} v_i = 0 \tag{35}$$

One equation remains. As a result, the eigenvalue 0 has multiplicity $M-1$, hence:

$$\text{rank}(\mathbf{G}(\boldsymbol{\theta}^*)) = 1 \tag{36}$$

This case corresponds to the square formation geometry, which is further discussed in III-C.

On the other hand, if $\exists j \in \{2,\dots,M\}$, such that $\sin(2\theta_j^* - 2\theta_1^*) \neq 0$, (34) becomes:

$$\begin{cases} \sum_{i=1}^{M} \cos(2\theta_1^* - 2\theta_i^*) v_i = 0 \\ \sum_{i=1}^{M} \sin(2\theta_1^* - 2\theta_i^*) v_i = 0 \end{cases} \tag{37}$$

resulting in 2 equations. The eigenvalue 0 has multiplicity $M-2$, giving:

$$\text{rank}(\mathbf{G}(\boldsymbol{\theta}^*)) = 2 \tag{38}$$

From (36) and (38), we conclude that:

$$\boxed{\text{rank}(\mathbf{G}(\boldsymbol{\theta}^*)) \leq 2} \tag{39}$$

### C. Proof of Theorem 1

Theorem 1 states that:

$$\begin{cases} \sum_{i=1}^{M} \cos^2(2\theta_i) = \frac{M}{2} \\ \sum_{i=1}^{M} \cos(2\theta_i)\sin(2\theta_i) = 0 \end{cases} \iff \lambda_{max} = \frac{16}{M^2} \tag{40}$$

*Proof.* ( $\Longrightarrow$ ) We consider a formation geometry $\boldsymbol{\theta} \in \mathbb{O}_M$ such that:

$$\begin{cases} \sum_{i=1}^{M} \cos^2(2\theta_i) = \frac{M}{2} \\ \sum_{i=1}^{M} \cos(2\theta_i)\sin(2\theta_i) = 0 \end{cases} \tag{41}$$

The maximal eigenvalue $\lambda_{max}$ of $\mathbf{G}(\boldsymbol{\theta})$ associated with the eigenvector $\mathbf{v}$ is obtained by solving:

$$\mathbf{G}(\boldsymbol{\theta})\mathbf{v} = \lambda_{max}\mathbf{v} \tag{42}$$

We introduce $\alpha = \frac{M^3}{32}\lambda_{max}$. Equation (42) is equivalent to:

$$\sum_{i=1}^{M} \cos(2\theta_j - 2\theta_i) v_i = \alpha v_j, \forall j \in \{1,\dots,M\} \tag{43}$$

Using the cosine difference formula, (43) becomes:

$$c_j \sum_{i=1}^{M} c_i v_i + s_j \sum_{i=1}^{M} s_i v_i = \alpha v_j, \forall j \in \{1,\dots,M\} \tag{44}$$

where $c_i = \cos(2\theta_i)$ and $s_i = \sin(2\theta_i)$. Expressing (44) in matrix form gives:

$$\begin{bmatrix} c_1 & s_1 \\ \vdots & \vdots \\ c_M & s_M \end{bmatrix} \begin{bmatrix} c_1 & \dots & c_M \\ s_1 & \dots & s_M \end{bmatrix} \mathbf{v} = \alpha \mathbf{v} \tag{45}$$

We select two rows indexed $i$ and $j$ of (45) for which $s_{ij} = \sin(2\theta_i - 2\theta_j) \neq 0$. Such a selection necessarily exists since $\boldsymbol{\theta}$ satisfies (41). Without loss of generality, we label the selected rows as 1 and 2. We get:

$$\begin{bmatrix} c_1 & s_1 \\ c_2 & s_2 \end{bmatrix} \begin{bmatrix} c_1 & \dots & c_M \\ s_1 & \dots & s_M \end{bmatrix} \mathbf{v} = \alpha \begin{bmatrix} v_1 \\ v_2 \end{bmatrix} \tag{46}$$

The first matrix of (46) is invertible as we have chosen $\theta_1$ and $\theta_2$ such that $s_{21} = \sin(2\theta_2 - 2\theta_1) \neq 0$. Then, we have:

$$\begin{bmatrix} c_1 & \dots & c_M \\ s_1 & \dots & s_M \end{bmatrix} \mathbf{v} = \frac{\alpha}{s_{21}} \begin{bmatrix} s_2 & -s_1 \\ -c_2 & c_1 \end{bmatrix} \begin{bmatrix} v_1 \\ v_2 \end{bmatrix} \tag{47}$$

Substituting (47) into (45) yields:

$$\frac{\alpha}{s_{21}} \begin{bmatrix} c_1 & s_1 \\ \vdots & \vdots \\ c_M & s_M \end{bmatrix} \begin{bmatrix} s_2 & -s_1 \\ -c_2 & c_1 \end{bmatrix} \begin{bmatrix} v_1 \\ v_2 \end{bmatrix} = \alpha \mathbf{v} \tag{48}$$

Using the sine difference formula, we get:

$$\mathbf{v} = \frac{1}{s_{21}} \begin{bmatrix} s_{21} & s_{11} \\ \vdots & \vdots \\ s_{2M} & s_{M1} \end{bmatrix} \begin{bmatrix} v_1 \\ v_2 \end{bmatrix} \tag{49}$$

By substituting (49) into (46), we obtain:

$$\alpha \begin{bmatrix} v_1 \\ v_2 \end{bmatrix} = \frac{1}{s_{21}} \begin{bmatrix} c_1 & s_1 \\ c_2 & s_2 \end{bmatrix} \begin{bmatrix} c_1 & \dots & c_M \\ s_1 & \dots & s_M \end{bmatrix} \begin{bmatrix} s_{21} & s_{11} \\ \vdots & \vdots \\ s_{2M} & s_{M1} \end{bmatrix} \begin{bmatrix} v_1 \\ v_2 \end{bmatrix} \tag{50}$$

Further computations of (50) give:

$$\alpha \begin{bmatrix} v_1 \\ v_2 \end{bmatrix} = \frac{1}{s_{21}} \begin{bmatrix} \sum_{i=1}^{M} c_{1i}s_{2i} & \sum_{i=1}^{M} c_{1i}s_{i1} \\ \sum_{i=1}^{M} c_{2i}s_{2i} & \sum_{i=1}^{M} c_{2i}s_{i1} \end{bmatrix} \begin{bmatrix} v_1 \\ v_2 \end{bmatrix} \tag{51}$$

We simplify (51), by developing each sum and using (41). We get:

$$\alpha \begin{bmatrix} v_1 \\ v_2 \end{bmatrix} = \frac{1}{s_{21}} \begin{bmatrix} s_{21}\frac{M}{2} & 0 \\ 0 & s_{21}\frac{M}{2} \end{bmatrix} \begin{bmatrix} v_1 \\ v_2 \end{bmatrix} \tag{52}$$

which leads to:

$$\boxed{\alpha = \frac{M}{2} \iff \lambda_{max} = \frac{16}{M^2}} \tag{53}$$

Equation (52) shows that $v_1$ and $v_2$ can be chosen independently because no relation links them. We substitute $[v_1, v_2]^\top$ with $[\cos(2\theta_1), \cos(2\theta_2)]^\top$ and then with $[\sin(2\theta_1), \sin(2\theta_2)]^\top$ into (51). We obtain two orthogonal eigenvectors $\mathbf{u}$ and $\mathbf{v}$ associated with $\lambda_{max}$:

$$\mathbf{u} = \begin{bmatrix} \cos 2\theta_1 \\ \vdots \\ \cos 2\theta_M \end{bmatrix} \quad \mathbf{v} = \begin{bmatrix} \sin 2\theta_1 \\ \vdots \\ \sin 2\theta_M \end{bmatrix} \tag{54}$$

□

*Proof.* ($\Longleftarrow$) Let $\boldsymbol{\theta}$ be a formation in $\mathbb{O}_M$ such that $\lambda_{max} = \frac{16}{M^2}$ is the non-null eigenvalue of $\mathbf{G}$ of multiplicity 2. We have then:

$$\begin{cases} \mathbf{G}.\mathbf{u} = \frac{16}{M^2}\mathbf{u} \\ \mathbf{G}.\mathbf{v} = \frac{16}{M^2}\mathbf{v} \end{cases} \tag{55}$$

where $\mathbf{u} \perp \mathbf{v}$ are two eigenvectors associated to $\lambda_{max}$. We choose:

$$\mathbf{u} = \begin{bmatrix} \cos 2\theta_1 \\ \vdots \\ \cos 2\theta_M \end{bmatrix} \text{ and } \mathbf{v} = \begin{bmatrix} \sin 2\theta_1 \\ \vdots \\ \sin 2\theta_M \end{bmatrix} \tag{56}$$

Substituting (56) into (55) yields:

$$\forall j \in \{2,\dots,M\},$$
$$\begin{cases} \frac{32}{M^3}\sum_{i=1}^{M}\cos(2\theta_j-2\theta_i)\cos(2\theta_i) = \frac{16}{M^2}\cos(2\theta_j) \\ \frac{32}{M^3}\sum_{i=1}^{M}\cos(2\theta_j-2\theta_i)\sin(2\theta_i) = \frac{16}{M^2}\sin(2\theta_j) \end{cases} \tag{57}$$

We can further simplify the system (57) using the product-to-sum formula for trigonometric functions:

$$\forall j \in \{2,\dots,M\},$$
$$\begin{cases} \frac{1}{2}\sum_{i=1}^{M}\left[\cos(2\theta_j)+\cos(2\theta_j-4\theta_i)\right] = \frac{M}{2}\cos(2\theta_j) \\ \frac{1}{2}\sum_{i=1}^{M}\left[\sin(2\theta_j)+\sin(2\theta_j-4\theta_i)\right] = \frac{M}{2}\sin(2\theta_j) \end{cases} \tag{58}$$

Using the formula for the cosine and sine of a difference, we obtain:

$$\forall j \in \{2,\dots,M\},$$
$$\begin{cases} \cos(2\theta_j)\sum_{i=1}^{M}\cos(4\theta_i)+\sin(2\theta_j)\sum_{i=1}^{M}\sin(4\theta_i) = 0 \\ \sin(2\theta_j)\sum_{i=1}^{M}\cos(4\theta_i)-\cos(2\theta_j)\sum_{i=1}^{M}\sin(4\theta_i) = 0 \end{cases} \tag{59}$$

The system (59) can be reformulated as:

$$\forall j \in \{2,\dots,M\},$$
$$\begin{cases} \begin{pmatrix}\cos(2\theta_j)\\ \sin(2\theta_j)\\ 0\end{pmatrix} \cdot \sum_{i=1}^{M}\begin{pmatrix}\cos(4\theta_i)\\ \sin(4\theta_i)\\ 0\end{pmatrix} = 0 \\ \left[\begin{pmatrix}\cos(2\theta_j)\\ \sin(2\theta_j)\\ 0\end{pmatrix} \times \sum_{i=1}^{M}\begin{pmatrix}\cos(4\theta_i)\\ \sin(4\theta_i)\\ 0\end{pmatrix}\right].\mathbf{e}_3 = 0 \end{cases} \tag{60}$$

Since two vectors can not be simultaneously normal and collinear and that $\begin{bmatrix}\cos(2\theta_j) & \sin(2\theta_j) & 0\end{bmatrix}^T \neq \mathbf{0}$, it is clear that solutions of (60) have to satisfy:

$$\begin{cases} \sum_{i=1}^{M}\cos(4\theta_i) = 0 \\ \sum_{i=1}^{M}\sin(4\theta_i) = 0 \end{cases} \iff \begin{cases} \sum_{i=1}^{M}\cos^2(2\theta_i) = \frac{M}{2} \\ \sum_{i=1}^{M}\cos(2\theta_i)\sin(2\theta_i) = 0 \end{cases} \tag{61}$$

□

### D. Computation of the Hessian Matrix $\frac{\partial^2 PDOP^2}{\partial \mathbf{q}^2}$

The Hessian matrix $\frac{\partial^2 PDOP^2}{\partial \mathbf{q}^2}$ in (26) is defined as:

$$\frac{\partial^2 PDOP^2}{\partial \mathbf{q}^2} = \begin{bmatrix} \frac{\partial^2 PDOP^2}{\partial x^2} & \frac{\partial^2 PDOP^2}{\partial xy} \\ \frac{\partial^2 PDOP^2}{\partial xy} & \frac{\partial^2 PDOP^2}{\partial y^2} \end{bmatrix} \tag{62}$$

Since (3) relates $\mathbf{q}$ with $\boldsymbol{\theta}$, we use the chain rule to compute each coefficient of the Hessian matrix from (30). We get:

$$\begin{cases} \frac{\partial^2 PDOP^2}{\partial x^2} = \frac{32}{M^3}\sum_{i=1}^{M}\frac{\sin^2\theta_i}{\rho_i^2} \\ \frac{\partial^2 PDOP^2}{\partial xy} = \frac{32}{M^3}\sum_{i=1}^{M}\frac{-\sin\theta_i\cos\theta_i}{\rho_i^2} \\ \frac{\partial^2 PDOP^2}{\partial y^2} = \frac{32}{M^3}\sum_{i=1}^{M}\frac{\cos^2\theta_i}{\rho_i^2} \end{cases} \tag{63}$$

which leads us, in matrix form, to (26).


## ACKNOWLEDGMENT

This project is funded and carried out within the framework of the SAMURAI project (ANR-21-CE33-0014).


## REFERENCES


[1] C. Hegarty and E. Kaplan. "Understanding GPS Principles and Applications, Second Edition," In *Artech*, 2006.

[2] M. Wang, Z. Chen, Z. Zhou, J. Fu and H. Qiu. "Analysis of the Applicability of Dilution of Precision in the Base Station Configuration Optimization of Ultrawideband Indoor TDOA Positioning System, " In *IEEE Access*, vol. 8, Dec 2020.

[3] G. Bellusci, G.J.M. Janssen, J. Yan and C.C.J.M. Tiberius. "Model of distance and bandwidth dependency of TOA-based UWB ranging error," In *IEEE International Conference on Ultra-Wideband*, pp. 193-196, Hannover, Germany, Sep 2008.

[4] M. Laguna , J.O. Roa , A.R. Jiménez and F. Seco. "Diversified local search for the optimal layout of beacons in an indoor positioning system," In *IIE Trans.*, vol. 41, no 3, pp.247-259, Jan 2009.

[5] L. Génevé, O. Kermorgant and É. Laroche. "Limits of Trilateration-Based Sensor Placement Algorithms," In *IEEE Sensors Applications Symposium*, Glassboro, United States, Mar 2017.

[6] W. Zhao, A. Goudar and A.P. Schoellig. "Finding the Right Place: Sensor Placement for UWB Time Difference of Arrival Localization in Cluttered Indoor Environments," In *IEEE Robotics and Automation Letters*, vol. 7, no. 3, pp. 6075-6082, Jul 2022.

[7] N. Megiddo and K.J. Supowit. "On the complexity of some common geometric location problems," In *SIAM Journal of Computing*, vol. 13, no. 1, pp. 182–196, Feb 1984.

[8] W. Zhao, M. Vukosavljev and A.P. Schoellig. "Optimal Geometry for Ultra-Wideband Localization using Bayesian Optimization," In *IFAC*, vol. 13, no. 1, p. 15481-15488, Jul 2020.

[9] S. Xue and Y. Yang. "Positioning Configurations with the Lowest GDOP and Their Classification," In *Journal of Geodesy*, vol. 89, no 1, Jan 2015.

[10] N. Levanon. "Lowest GDOP in 2-D scenarios," In *IEEE Proceedings - Radar, Sonar and Navigation*, vol. 146, no 3, p. 149, Jun 2000.

[11] P. Krapež and M. Munih. "Anchor Calibration for Real-Time-Measurement Localization Systems," In *IEEE Trans. on Instrumentation and Measurement*, vol. 69, no. 12, pp. 9907-9917, Dec. 2020.

[12] Y. Zou, C. Wang, J. Zhu, and Q. Li. "Optimal sensor configuration for positioning seafloor geodetic node," In *Ocean Eng.*, vol. 142, 2017.

[13] D. Moreno-Salinas, A.M. Pascoal and J. Aranda. "Optimal sensor placement for underwater positioning with uncertainty in the target location," In *ICRA*, Shanghai, China, pp. 2308-2314, May 2011.

[14] L. Heng and G.X. Gao. "Accuracy of Range-Based Cooperative Positioning: A Lower Bound Analysis," In *IEEE Trans. on Aerospace and Electronic Systems*, vol. 53, no. 5, pp. 2304-2316, Oct. 2017.

[15] A.N. Bishop, B. Fidan, B.D.O. Anderson, K. Doğançay, P.N. Pathirana. "Optimality analysis of sensor-target localization geometries," In *Automatica*, vol. 46, Issue 3, p.479-492, Mar 2010.

[16] S. Martínez and F. Bullo. "Optimal sensor placement and motion coordination for target tracking," In *Automatica*, vol. 42, Issue 4, p.661-668, Apr 2006.

[17] S. Zhao and B.M. Chen. "Optimal Sensor Placement for Target Localisation and Tracking in 2D and 3D"," In *International Journal of Control*, vol. 86, no 10, p. 1687-704, Oct 2013.

[18] L. Zhang, Z. Zhang, R. Siegwart and J.J. Chung. "Distributed PDOP Coverage Control: Providing Large-Scale Positioning Service Using a Multi-Robot System," In *IEEE Robotics and Automation Letters*, vol. 6, no 2, p. 2217-24, Apr 2021.

[19] J. Cano, G. Pages, E. Chaumette and J. Le Ny. "Optimal Localizability Criterion for Positioning with Distance-Deteriorated Relative Measurements," In *IEEE/RSJ IROS*, p. 947-53, Oct 2022.

[20] H. Lee. "Accuracy Limitations of Hyperbolic Multilateration Systems," In *IEEE Trans. on Aerospace and Electronic Systems*, vol. 11, no. 1, pp. 16-29, Jan 1975.

[21] J. González, J.L. Blanco, C. Galindo, A. Ortiz-de-Galisteo, J.A. Fernández-Madrigal, F.A. Moreno, J.L. Martínez. "Mobile Robot Localization Based on Ultra-Wide-Band Ranging: A Particle Filter Approach," In *Robotics and Autonomous Systems*, vol. 57, no 5, p. 496-507, May 2009.

[22] Z. Qin, J. Wang and S. Wei. "A study of 3D sensor array geometry for TDOA based localization," In *CIE International Conference on Radar (RADAR)*, Guangzhou, China, pp. 1-5, Oct 2016.